Supporting Information: Influence of Conductive Additives and Binder on the Impedance of Lithium-Ion Battery Electrodes: Effect of an Inhomogeneous Distribution

Mrudula Prasad[a,b], Simon Hein[a,b], Timo Danner[a,b,*], Benedikt Prifling[c], Rares Scurtu[d], Alice Hoffmann[d], André Hilger[e], Markus Osenberg[e], Ingo Manke[e], Margret Wohlfahrt-Mehrens[d], Volker Schmidt[c], Arnulf Latz[a,b,f]

[a] *German Aerospace Center (DLR), Institute of Engineering Thermodynamics,Pfaffenwaldring 38-40,70569 Stuttgart, Germany*
[b] *Helmholtz-Institut Ulm für Elektrochemische Energiespeicherung (HIU), Helmholtzstraße 11, 89081 Ulm, Germany*
[c] *Ulm University (UUlm), Institute of Stochastics, Helmholtzstraße 18, 89081 Ulm, Germany*
[d] *ZSW-Zentrum für Sonnenenergie- und Wasserstoff-Forschung Baden-Württemberg, Helmholtzstraße 8,89081 Ulm, Germany*
[e] *Helmholtz-Zentrum Berlin für Materialien und Energie, Hahn-Meitner-Platz 1, 14109 Berlin, Germany*
[f] *Ulm University (UUlm), Institute of Electrochemistry, Albert-Einstein-Allee 47, 89081 Ulm, Germany*

SI 1. Electrochemical parameters

The electrochemical parameters used for the microstructure-resolved simulations and their respective references are listed in Table SI-1.

The effect of the separator and the CBD phase on the transport in the electrolyte is included into the electrochemical simulations through reduced diffusion and conductivity coefficients. Transport in the separator is reduced by the Bruggeman coefficient (Equation SI-1) [3], where τ is the corrected

*Corresponding author:
Email address: timo.danner@dlr.de (Timo Danner)
URL: http://www.dlr.de/tt/en/ (Timo Danner)

tortuosity, β is the exponent, and ϵ is the particle porosity.

$$\tau = \epsilon^{1-\beta} \tag{SI-1}$$

Further amendments to this correction was made depending on the density of the CBD phase in the electrode. This is summarised in Table SI-1.

Table SI-1: Model parameters used for the electrochemical simulations.

Parameter/units	Description	Value	Source
Electrolyte: LiPF6 in EC:EMC			
c_{El}^{ini} / [mol/m^3]	Initial concentration of Li salt	10^3	[1]
D_{El} / m^2 s^{-1}	Li-ion diffusion coefficient	fit to data in	[10]
κ_{El} / S m^{-1}	Ion conductivity	fit to data in	[10]
$f_{\pm}$ / -	Thermodynamic factor	fit to data in	[10]
$t_{\pm}$ / -	Transference number	fit to data in	[10]
Active material cathode: NMC622			
c_{NMC}^{max} / mol m^{-3}	Max Li concentration	50451	[12]
c_{NMC}^{ini} / mol m^{-3} (SYM-EIS)	Initial Li concentration	50446	[a]
c_{NMC}^{ini} / mol m^{-3} (HC)	Initial Li concentration	35991	[b]
D_{NMC} / m^2 s^{-1}	Li-ion diffusion coefficient	fit to data in	[11]
σ_{NMC} / S m^{-1} (SYM-EIS)	Electric conductivity	1×10^{-2}	[c]
σ_{NMC} / S m^{-1} (HC)	Electric conductivity	fit to data in	[11]
U_{NMC} / V	Open circuit potential	fit to data in	[11]
i_{Inter}^{00} / A m mol^{-1} (SYM-EIS)	Exchange current density	2.3047×10^{-6}	[d]
i_{Inter}^{00} / A m mol^{-1} (HC)	Exchange current density	2.3047×10^{-3}	[2]
C_{DL}^{NMC} / F m^{-2}	Double-layer capacitance	2.4	[12]
Transport parameters in CBD			
τ / -	Tortuosity	4.12	[e]
ϵ / -	Nanoporosity	50%	[14]
$\kappa_{CBD_{Bulk}}$ / S m^{-1}	Ion conductivity (bulk)	$\frac{\epsilon}{\tau}\ \kappa_{El}$	[e]
$\kappa_{CBD_{Dense}}$ / S m^{-1}	Ion conductivity (dense)	$0.1 \times \kappa_{CBD_{Bulk}}$	Assumed
$\sigma_{CBD_{Bulk}}$ / S m^{-1}	Electric conductivity (bulk)	10^2	Assumed
$\sigma_{CBD_{Dense}}$ / S m^{-1}	Electric conductivity (dense)	$2 \times \sigma_{CBD_{Bulk}}$	Assumed
Counter-Electrode: Lithium			
D_{NMC} / m^2 s^{-1}	Li-ion diffusion coefficient	10^4	Assumed
c^{ini} / mol m^{-3} (HC)	Initial Li concentration	N/A	[f]
σ_{CE} / S m^{-1}	Electric conductivity	10	[1]
i_{CE}^{00} / A m^{-2}	Exchange current density	3.64×10^2	[13]
C_{DL}^{CE} / F m^{-2}	Double-layer capacitance	1.0	Assumed
Current Collector (CC)			
σ_{CC} / S m^{-1}	Electric conductivity	10^4	Assumed
Separator			
β / - (Equation SI-1)	Bruggeman exponent	1.5	For spheres
ϵ / -	Nanoporosity	50%	[12]
τ / -	Tortuosity	$\epsilon^{(1-\beta)}$	[12]
$\kappa_{Separator}$ / S m^{-1}	Ion conductivity	$\frac{\epsilon}{\tau}\ \kappa_{El}$	[12]

The data fit functions are given in [1]. [a] value was chosen close to complete lithiation to ensure blocking electrolyte conditions. [b] value chosen was at 50% depth-of-discharge matching the experimental initial conditions. [c] was assumed to be larger than [11] to ensure numerical convergence. [d] value for symmetric cell impedance (SYM-EIS) was lower than [2] to ensure blocking electrolyte conditions. [e] value as specified for two-layer EDX-closed electrodes [14]. [f] model setting is a near infinite concentration of Li-ion at the anode-electrolyte interface.

SI 2. Density calculation

The densities and the mass fractions of the active material, the conductive additives and the binder in the dry electrode before calendaring are listed in Table SI-2. The density of the solid part of the electrode is calculated according to

$$\rho_E^s = \frac{1}{\sum_i \frac{w_i}{\rho_i}} \ , \tag{SI-2}$$

where w_i is the mass fraction and ρ_i , the density of each component. The porosity of the electrode can be calculated from the solid density ρ_E^s as

$$\epsilon_{Pore} = 1 - \frac{\rho_E}{\rho_E^s} = 1 - \epsilon_{Solid} \ . \tag{SI-3}$$

The volume fraction of each component can be obtained through

$$\epsilon_i = \frac{w_i}{\rho_i} \cdot \rho_E^s \cdot \epsilon_{Solid} \ . \tag{SI-4}$$

The calculated volume fractions of each component are listed in the last column of Table SI-2.

Table SI-2: Densities, mass fractions and volume fractions of each component of the electrode.

Material	Density	Mass fraction	Volume fraction
NMC622	4780 kg/m^3	93 wt-%	58.3 vol-%
Binder	1780 kg/m^3	4 wt-%	6.7 vol-%
Carbon black	1850 kg/m^3	2 wt-%	3.2 vol-%
Graphite	2260 kg/m^3	1 wt-%	1.3 vol-%

The total volume fraction of the CBD before calendaring is thus 11.2 vol.-%.

SI 3. Intermediate results - structural characterisation

In this work we consider five unique CBD configurations at three different electrode densities, and three cutouts at each density. In the following subsections, the volume fraction distribution, specific surface area (SSA), and electronic as well as ionic conductivities of the various electrodes are shown.

SI 3.1. Volume fraction and specific surface area (SSA)

Figure SI-1 (a) shows the volume fraction distribution across the electrode thickness, and (b) illustrates the SSA for each configuration under the three different electrode densities. The SSA was calculated using GeoDict [1]. The SSA (SSA_{Total}) calculation (Figure SI-1 (b)) takes the porosity of the CBD into account, which reduces the contact between the cathode AM and the electrolyte: $SSA_{Total} = SSA_{AM} + 0.5 \cdot SSA_{CBD}$. For Figure SI-1 (a), only the "Homogeneous" configuration is shown, where the CBD distribution is uniform across the electrode thickness.

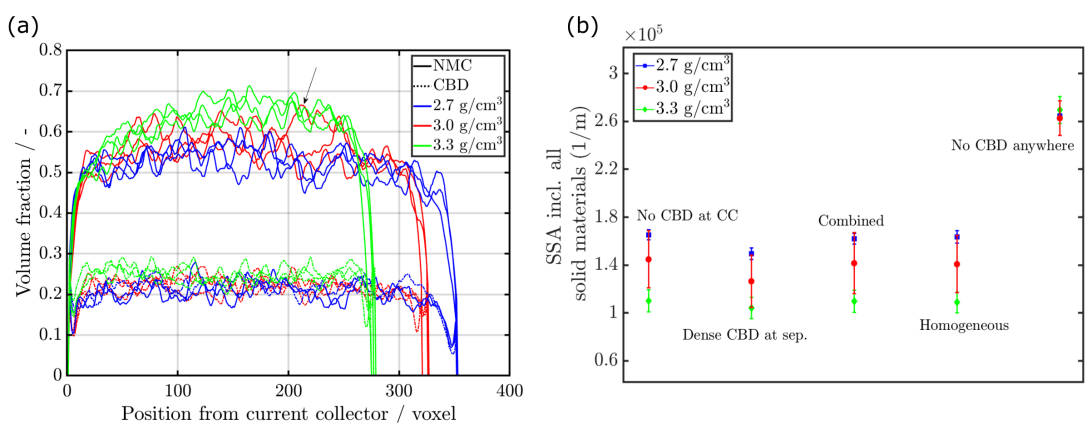

Figure SI-1: Illustrates the geometric properties of the electrodes with densities 2.7, 3.0 and 3.3 /cm^3. In (a) the volume fraction plot of AM and CBD distribution across the 3 electrode densities for the "Homogeneous" case. The voxel size is 438 nm. And in (b) the specific surface area (SSA) of the electrodes for the different configurations and densities.

It can be seen from Figure SI-1 (a), that within the same electrode density, the reconstructions show a low deviation from one another. The 3.0 g/cm^3

[1] GeoDict simulation software Release 2023, by Math2Market GmbH, Germany, doi.org/10.30423/release.geodict2023

electrode exhibits the largest standard deviation amongst the three electrode densities (indicated in the black arrow). This is in line with the cathode AM fluctuations shown in Figure SI-1 (a). This highlights the need to consider several electrode cutouts for the simulations. The lowest total solid volume fraction is observed in the electrode with the least calendered density (2.7 g/cm^3). Overall, the different scenarios including CBD show a similar active surface area, eventhough we did not enforce the same CBD content (see Table SI-3 for the volume fractions of the CBD in the different scenarios). This indicates that impact on intercalation and charge transfer resistance can be expected to be minor. In contract, the case without CBD shows a significantly higher SSA.

Table SI-3: Summary of the average fractions of cathode AM, pore space and CBD in each configuration for all three electrode densities. The pore space volume fraction does not include the CBD nanoporosity.

Average volume fraction of/ in configuration	AM	Pore	CBD
2.7 g/cm^3 electrode			
No CBD at CC	0.50	0.27	0.22
Dense CBD at sep.	0.52	0.24	0.24
Combined	0.51	0.23	0.26
Homogeneous	0.52	0.27	0.21
No CBD anywhere	0.52	0.48	0
3.0 g/cm^3 electrode			
No CBD at CC	0.53	0.24	0.23
Dense CBD at sep.	0.55	0.20	0.25
Combined	0.53	0.23	0.24
Homogeneous	0.55	0.23	0.22
No CBD anywhere	0.55	0.45	0
3.3 g/cm^3 electrode			
No CBD at CC	0.63	0.13	0.25
Dense CBD at sep.	0.63	0.11	0.26
Combined	0.63	0.12	0.25
Homogeneous	0.63	0.13	0.25
No CBD anywhere	0.63	0.37	0

SI 3.2. Electronic and ionic conductivities

As shown in Figure SI-2, the ionic and electronic conductivities not only differ between the three electrode densities, but also within the five CBD

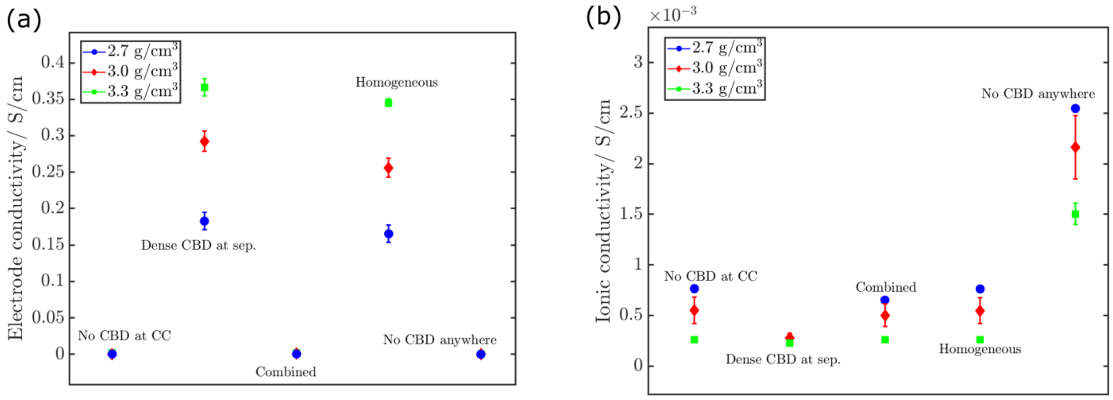

Figure SI-2: Shows the (a) electronic and (b) ionic conductivities of the different CBD geometries for the several electrode densities and their cutouts.

geometries. However, there are some common denominators between the several configurations, allowing us to identify what the dominating non-uniformity is. For example, in cases "No CBD at CC", "Combined" and "No CBD anywhere", the electronic conductivities at varying electrode densities are proximate to one another, due to the common denominator of a loss of a percolating conductive additive network. Even small layers with pure cathode AM conductivity reduce the effective conductivity significantly. In the same manner, dense accumulation of binder at the separator reduces the effective ionic conductivity, especially in the "Dense CBD at sep." scenario. However, this effect is less pronounced compared to the effective electronic conductivity. The best ion transport, on the other hand, occurs in the "No CBD anywhere" electrode. Other than that, the electronic and ionic transport in the "Homogeneous" case is one of the highest at all electrode densities.

From Figure SI-2 (b), the optimum ionic pathways are present in electrodes calendered to a lower density. On the contrary, higher electrode densities exhibit enhanced electronic pathways owing to better particle-particle and electrode-CC contact, leading to an increased effective electronic conductivity (Figure SI-2 (a)). As the main impedance to ion transport into the electrode is the enriched binder at the surface of the "Dense CBD at sep." case, all the electrode densities show low ion conductivities for this configuration. This is also translated to the HC delithiation simulations, where all the electrode densities perform similarly in the "Dense CBD at sep." configuration while showing large capacity differences in the "No CBD anywhere"

case (see Figure SI-5).

SI 4. Additional Figures

SI 4.1. Effect of kinetic constants on the high-frequency semi-circle

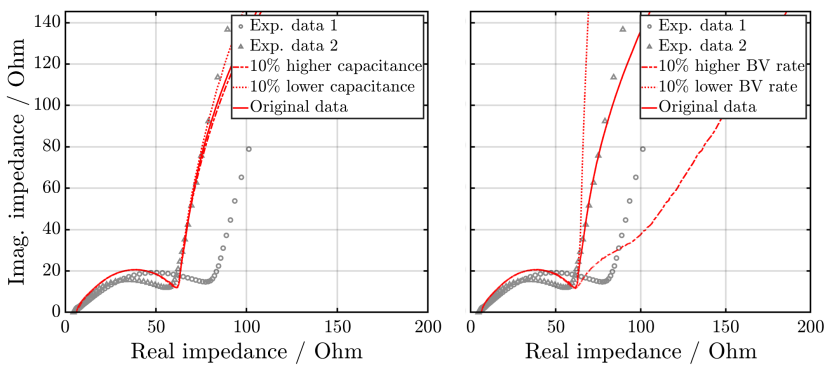

Figure SI-3: Show the influence of changes in the double-layer capacitance and Butler-Volmer (BV) kinetic constant on the high-frequency semi-circle for the "Combined" configuration at 3.0 g/cm^3. The experimental measurements and simulations were both conducting under blocking electrolyte conditions.

As seen from Figure SI-3, changing the kinetic constants did not affect the magnitude of the impedances recorded at high frequencies. A factor of 10% is an arbitrarily chosen value for investigative purposes.

SI 4.2. Symmetric cell and HC simulation results for all electrode densities at all cutouts

SI 4.2.1. Symmetric cell EIS data

Figure SI-4 shows the impedance simulations and experimental data at 2.7, 3.0 and 3.3 g/cm^3 electrode densities. Eventhough, the electronic conductivity seems to contribute more to the differences in effective conductivities between the several configurations and calendered densities (see Figure SI-2), the impedances show that although this has a higher impact on the real part, the ionic conductivity influences the imaginary part. Hence, a combination of both effects is expected to be present. The "Combined" scenario seems to best fit with the experimental data at all electrode densities. However, the effective transport parameters used for the bulk CBD phase seem

to underestimate the ionic transport within the electrode for the 3.3 g/cm^3 electrode, resulting in an imaginary impedance higher than the experimental data for all configurations. The heterogeneous layers were adjusted to the minimum setting, yet it did not agree with the measurements to the same degree as at the other electrode densities. Lower porous volume at higher calendered densities, combined with low effective ion transport, may have led to overestimating the pore transport impedance.

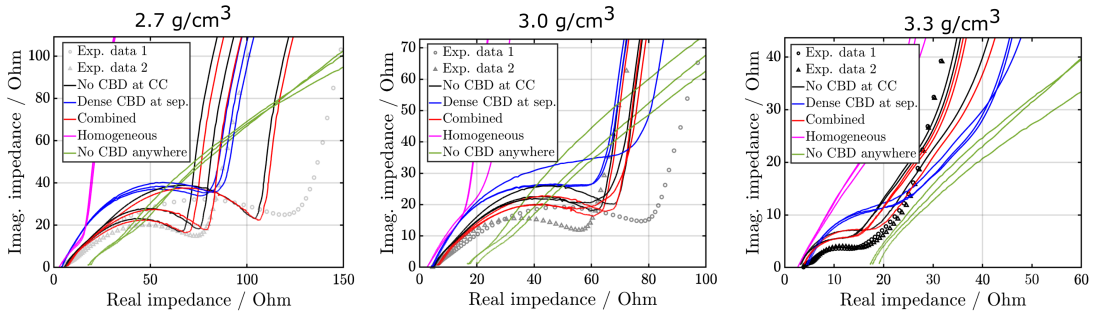

Figure SI-4: Shows the symmetric impedance experimental data and simulation results for all cutouts for all electrode densities under blocking electrolyte conditions.

SI 4.2.2. HC discharge data

Figure SI-5 shows the HC delithiation simulation results for all electrode densities at all cutouts for all discharge currents. The practical capacities are normalised according to the values provided in Table SI-4.

Table SI-4: Summarises the average theoretical capacities of the experiments ("Exp.") and cutouts of tomographic image data ("Tomo.") for all the three electrode densities. "TC" stands for theoretical capaciy.

Electrode density g/cm^3	TC (Exp.) mAh/cm^2	TC (Tomo.) mAh/cm^2
2.7	7.10	7.29 ± 0.03
3.0	7.30	7.15 ± 0.27
3.3	7.29	6.74 ± 0.10

We can see from Figure SI-5 that the trend showcased by all the configurations is identical across all electrode densities. The "Combined" case best represents the experimental data, while the "No CBD anywhere" shows the highest capacities at high C-rates. Figure SI-6 (b) shows that at low

C-rates, the solid conduction network is the limiting factor, as even with the ample electrolyte distribution (corresponding Figure SI-6 (a)), the "No CBD anywhere" still shows reduced cathode AM lithiation. Whereas for the other cases, even the centers of the cathode AM particles are lithiated. With increasing C-rates, however, the absence of a tortuous ion transport pathway allows the "No CBD anywhere" to maintain the capacities delivered.

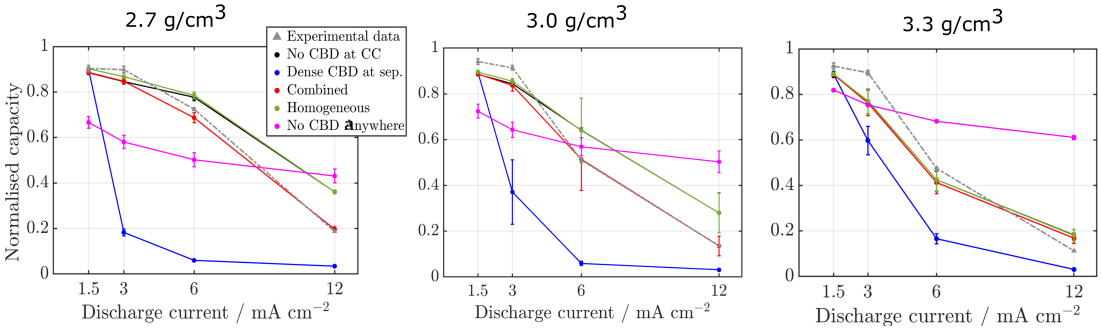

Figure SI-5: Shows the HC discharge simulations for all cutouts at all discharge currents for all electrode densities. The discharge capacities were normalised to their nominal data at the lower cut-off (3.0 V) voltage.

However, there is an optimum for calendaring density: when the electrode mesoporous space is too limiting, the performance of the electrodes seem to be decoupled from the CBD distribution, as seen for 3.3 g/cm^3 in Figure SI-5. However, calendering the electrodes leads to compressing the microstructural defects that reduces, most importantly, the critical impedance to lithium-ion transport at the electrode-separator interface. Figure SI-7 shows, that at higher current densities, the extent of cathode AM utilisation is similar at all electrode densities. However, at lower current densities, the lower electrode densities exhibit a better AM utilisation, as seen in Figure 15 of the main text.

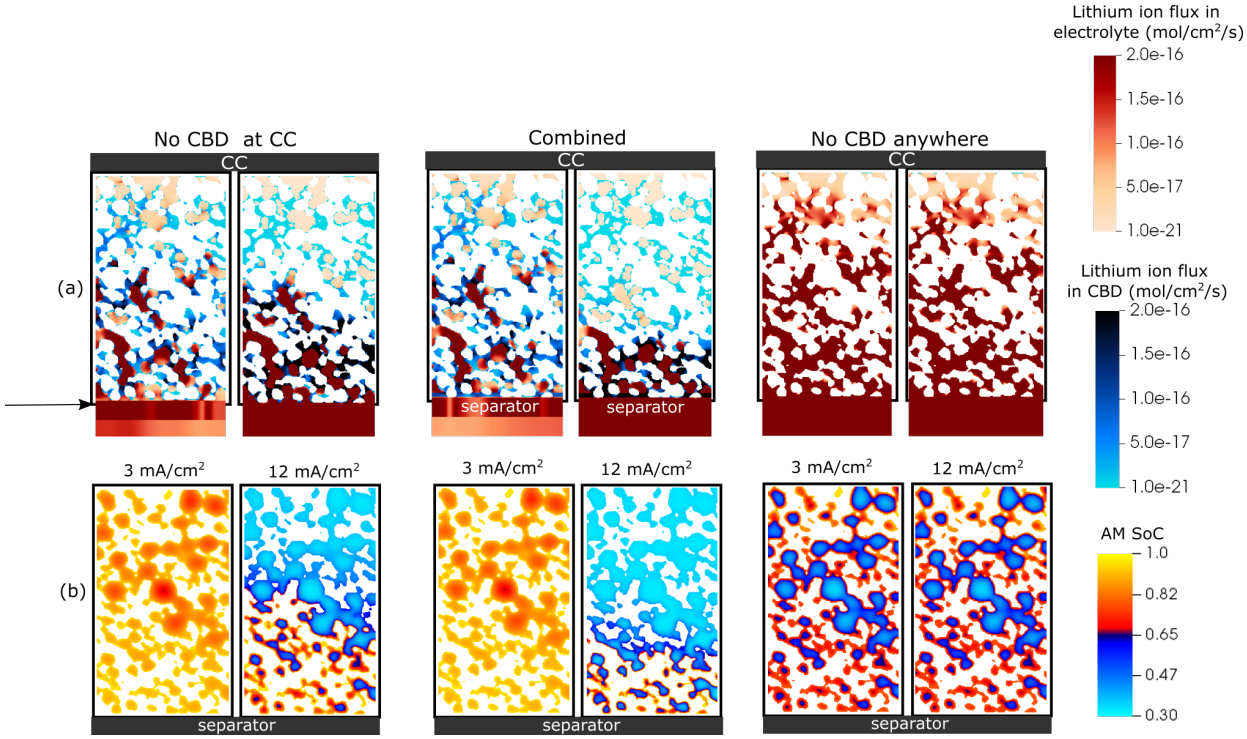

Figure SI-6: (a) separately shows the lithium-ion distribution within the CBD (in the orange colour scale) and mesoporous space (in the blue colour scale), and (b) shows the cathode AM state-of-charge (SoC) distribution across the thickness of the 3.0 g/cm^3 electrode. The slices were extracted at 3 mA/cm^2 and 12 mA/cm^2 at the lower cut-off (3.0V) of a lithiation simulation at half the electrode thickness, for three different configurations as labelled within the image.

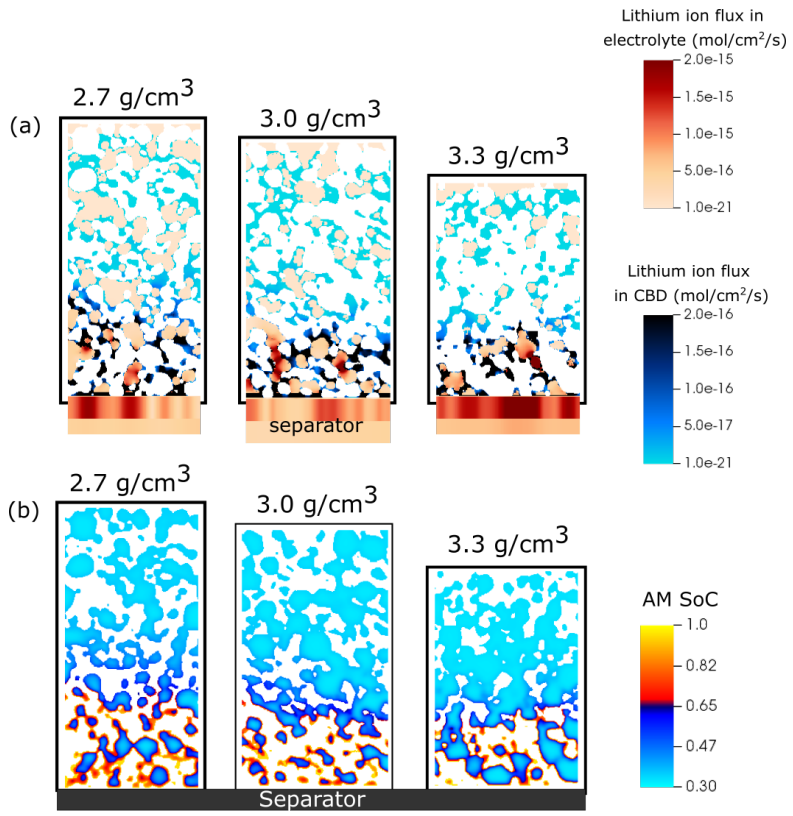

Figure SI-7: (a) separately shows the electrolyte distribution within the CBD (in the orange colour scale) and pore space (in the blue colour scale), and (b) extent of cathode AM lithiation for the "Combined" scenario at 12 mA/cm^2 for all electrode densities. The 2D slices were extracted at the lower cut-off (3.0 V) of a lithiation simulation at half the electrode thickness.

SI 5. References

[1] L. Kremer, A. Hoffmann, T. Danner, S. Hein, B. Prifling, D. Westhoff, C. Dreer, A. Latz, V. Schmidt, M. Wohlfahrt-Mehrens, Manufacturing process for improved ultra-thick cathodes in high-energy lithium-ion batteries, Energy Technology 8 (8) (2019) 1900167.

[2] L. Kremer, T. Danner, S. Hein, A. Hoffmann, B. Prifling, V. Schmidt, A. Latz, M. Wohlfahrt-Mehrens, Influence of the electrolyte salt concentration on the rate capability of ultra-thick NCM 622 electrodes, Batteries & Supercaps 3 (11) (2020) 1172-1182.

[3] J. Landesfeind, J. Hattendorff, A. Ehrl, W. A. Wall, H. A. Gasteiger, Tortuosity determination of battery electrodes and separators by impedance spectroscopy, Journal of The Electrochemical Society 163 (7) (2016) A1373–A1387.

[4] D. Westhoff, I. Manke, V. Schmidt, Generation of virtual lithium-ion battery electrode microstructures based on spatial stochastic modeling, Computational Materials Science 151 (2018) 53–64.

[5] A. Bezrukov, M. Bargieł, D. Stoyan, Statistical analysis of simulated random packings of spheres, Particle & Particle Systems Characterization 19 (2) (2002) 111–118.

[6] J. Feinauer, A. Spettl, I. Manke, S. Strege, A. Kwade, A. Pott, V. Schmidt, Structural characterization of particle systems using spherical harmonics, Materials Characterization 106 (2015) 123–133.

[7] B. Münch, L. Holzer, Contradicting geometrical concepts in pore size analysis attained with electron microscopy and mercury intrusion, Journal of the American Ceramic Society 91 (12) (2008) 4059–4067.

[8] J. Ohser, F. Mücklich, Statistical analysis of microstructures in materials science, J. Wiley & Sons, Chichester, 2000.

[9] M. Neumann, C. Hirsch, J. Staněk, V. Beneš, V. Schmidt, Estimation of geodesic tortuosity and constrictivity in stationary random closed sets, Scandinavian Journal of Statistics 46 (3) (2019) 848–884.

[10] A. Nyman, M. Behm, G. Lindbergh, Electrochemical characterisation and modelling of the mass transport phenomena in $LiPF_6$-EC-EMC electrolyte, Electrochemica Acta 53 (22) (2008) 6356–6365.

[11] R. Amin, Y. Chiang, Characterization of electronic and ionic transport in $Li_{1-x}Ni_{0.33}Mn_{0.33}Co_{0.33}O_2$ (NMC333) and $Li_{1-x}Ni_{0.50}Mn_{0.20}Co_{0.30}O_2$ (NMC523) as a function of Li content, Journal of The Electrochemical Society 163 (8) (2016) A1512–A1517.

[12] S. Hein, T. Danner, D. Westhoff, B. Prifling, R. Scurtu, L. Kremer, A. Hoffmann, A. Hilger, M. Osenberg, I. Manke, M. Wohlfahrt-Mehrens, V. Schmidt, A. Latz, Influence of conductive additives and binder on the impedance of lithium-ion battery electrodes: Effect of morphology, Journal of The Electrochemical Society 167 (1) (2020) 013546.

[13] S.G. Meibuhr, Electrode studies in nonaqueous electrolytes, The Electrochemical Society 117 (1) (1970) 56.

[14] B. Prifling, M. Neumann, S. Hein, T. Danner, E. Heider, A. Hoffmann, P. Rieder, A. Hilger, M. Osenberg, I. Manke, M. Wohlfahrt-Mehrens, A. Latz, V. Schmidt, Quantitative comparison of different approaches for reconstructing the carbon-binder domain from tomographic image data of cathodes in lithium-ion batteries and its influence on electrochemical properties, Energy Technology 11 (5) (2023) 2200784.